Forward modeling of space-borne gravitational wave detectors

Louis J. Rubbo, Neil J. Cornish, and Olivier Poujade
Department of Physics, Montana State University, Bozeman, Montana 59717, USA
(Received 24 November 2003; published 20 April 2004)

Planning is underway for several space-borne gravitational wave observatories to be built in the next 10 to 20 years. Realistic and efficient forward modeling will play a key role in the design and operation of these observatories. Space-borne interferometric gravitational wave detectors operate very differently from their ground-based counterparts. Complex orbital motion, virtual interferometry, and finite size effects complicate the description of space-based systems, while nonlinear control systems complicate the description of ground-based systems. Here we explore the forward modeling of space-based gravitational wave detectors and introduce an adiabatic approximation to the detector response that significantly extends the range of the standard low frequency approximation. The adiabatic approximation will aid in the development of data analysis techniques, and improve the modeling of astrophysical parameter extraction.

DOI: 10.1103/PhysRevD.69.082003 PACS number(s): 04.80.Nn, 95.75.−z

I. INTRODUCTION

Gravitational wave astronomy can be broadly divided into high and low frequency bands, with the dividing line near 1 Hz. Seismic and gravity gradient noise prevent ground-based detectors from exploring the low frequency portion of the spectrum, making this source-rich region the sole preserve of space-based observatories.

Ground- and space-based interferometric gravitational wave detectors operate according to the same general principles, but differ in their implementation. Ground-based detectors, such as the Laser Interferometer Gravitational Wave Observatory (LIGO) [1], operate in the low frequency limit, where the wavelength of the gravitational waves is considerably larger than the size of the detector, and most sources are only in-band for a fraction of a second. These considerations simplify the description of the detector response, which may be well approximated by a quadrupole antenna moving at constant velocity with respect to the gravitational wave source. However, ground-based interferometers employ quasi-fixed rather than freely moving test masses, and the output of the detector is given by the response of the control loop used to keep the interferometer on a dark fringe. This complicates forward modeling efforts for ground-based detectors [2] as it makes the detector response non-linear. The situation with space-borne detectors is completely the opposite. Space-based detectors, such as the proposed Laser Interferometer Space Antenna (LISA) [3], will be able to detect gravitational waves with wavelengths that range from many times larger than the interferometer to many times smaller, and most sources will be in-band for months or years, so that the detector's orbital motion will impart amplitude, frequency, and phase modulations. These effects give rise to a complicated, time-dependent detector response function [4]. Space-borne detectors typically have large arm-lengths (5×10^9 m for LISA) that vary with time, which prevents them from operating as traditional interferometers. Instead, the interferometer signals are produced in software from phase differences measured in the detector using a procedure known as time delay interferometry (TDI) [5]. Despite these complications, the detector response remains linear, which greatly simplifies forward modeling efforts.

Forward modeling plays a key role in the design of any new scientific instrument, and is especially important when the instrument is the first of its kind. Work is now underway to produce an end-to-end model of the LISA observatory [6]. Key ingredients include accurate modeling of the spacecraft orbits and photon trajectories (this includes the effects of gravitational waves), realistic simulations of the time delay interferometry used to cancel laser phase noise, and experimental characterization of the various noise contributions. A good end-to-end model can help to make design trade offs, and to avoid costly mistakes. Forward modeling can also be used to develop and test data analysis strategies. While we focus our attention on LISA, our forward model can be used to study other proposals for space-borne gravitational wave detectors, such as the Big Bang Observatory [7].

Work on various elements of the LISA end-to-end model have been under development for some time. Modeling of the detector response has its roots in the Doppler tracking of spacecraft [8]. Results were initially derived for a static array with equal arm lengths [9,10]. Following the discovery of time delay interferometry [5], these results were extended to a static array with unequal arm lengths [5,11,12]. The orbital motion of the array was first incorporated in the low frequency limit [13], and later extended to the full detector response [4]. With the full response function in hand, we have developed an open source software package called *The LISA Simulator* [14] that takes as its input an arbitrary gravitational wave and returns as its output the simulated response of the LISA observatory. The main purpose of *The LISA Simulator* is to aid in the development of data analysis tools [13,15–17], but its modular design allows it to be extended into a full end-to-end model. For example, the static modeling [18] of the TDI implementation could be incorporated into *The LISA Simulator*, as could more realistic spacecraft orbits and experimentally determined noise spectra.

The value of a realistic end-to-end model has already become apparent with the discovery of flaws in the initial TDI scheme caused by the rotation of the array [19], time depen-

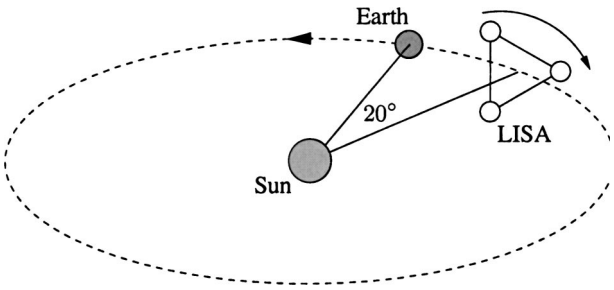

FIG. 1. The LISA mission configuration. The dashed line represents the orbit of the guiding center, which has a radius of 1 AU.

dence of the arm lengths [20], and problems with clock synchronization in a moving array [21]. These difficulties require modification of the TDI variables [19,20,22] and/or changes in the mission design.

On the other hand, a highly realistic end-to-end simulation necessarily consumes a great deal of computer resources, and delivers a fidelity that exceeds the requirements of many data analysis efforts. Indeed, when searching a large parameter space, fidelity must be sacrificed in favor of speed. To this end we have developed an approximation to the full LISA response that extends the low frequency approximation by two decades. The motion of the array is stroboscopically rendered into a sequence of stationary states, yielding an adiabatic approximation to the full response. The adiabatic approximation allows us to write down a simple analytic expression for the response function in a mixed time/frequency representation. For sources with a few dominant harmonics, such as low eccentricity, low spin binary systems at second post-Newtonian order, the adiabatic approximation provides a fast and accurate method for calculating the LISA response.

The outline of this paper is as follows. In Sec. II we describe the orbits of the interferometer constellation and describe how various effects enter into the detector response. In Sec. III we review the expression for the complete response of a space-borne detector. (An alternative derivation of the full response is given in Appendix B.) In Sec. IV we show some applications of the general formalism using *The LISA Simulator*. In Sec. V we explore the limitations of the low frequency approximation, and in Sec. VI we introduce the adiabatic approximation and demonstrate its utility. We finish with an application, using the adiabatic approximation to determine when LISA can detect the time evolution of a binary system. We work in natural units with $G=c=h=1$, but report all frequencies in Hertz.

II. SPACE-BORNE DETECTORS

A. Orbital effects

The current design of the LISA mission calls for three identical spacecraft flying in an equilateral triangular formation about the Sun. The center of mass for the constellation, known as the guiding center, is in a circular orbit at 1 AU. and 20° behind the Earth. In addition to the guiding center motion, the formation will cartwheel in a retrograde motion with a one year period (see Fig. 1). The detector motion introduces amplitude (AM), frequency (FM), and phase modulations (PM) into the gravitational wave signals [13,17]. The amplitude modulation is caused by the antenna pattern being swept across the sky. The phase modulation occurs when the differing responses to the two gravitational wave polarizations are combined together. The frequency (Doppler) modulation is due to the motion of the detector relative to the source. Since both the orbital and cartwheel motion have a period of one year, these modulations will show up as sidebands in the power spectrum separated from the instantaneous carrier frequency by integer values of the modulation frequency, $f_m = 1/\mathrm{yr}$.

To describe the coordinates of the detector we work in a heliocentric, ecliptic coordinate system. In this system the Sun is placed at the origin, the x axis points in the direction of the vernal equinox, the z axis is parallel to the orbital angular momentum vector of the Earth, and the y axis is placed in the ecliptic to complete the right-handed coordinate system. Ignoring the influence from other solar system bodies, the individual LISA spacecraft will follow independent Keplerian orbits. The triangular formation comes about through the judicious selection of initial conditions. In Appendix A we derive the spacecraft positions as a function of time. To second order in the eccentricity, the Cartesian coordinates of the spacecraft are given by

$$\begin{aligned} x(t) &= R\cos(\alpha) + \frac{1}{2}eR[\cos(2\alpha-\beta) - 3\cos(\beta)] \\ &\quad + \frac{1}{8}e^2R[3\cos(3\alpha-2\beta) - 10\cos(\alpha) \\ &\quad - 5\cos(\alpha-2\beta)] \\ y(t) &= R\sin(\alpha) + \frac{1}{2}eR[\sin(2\alpha-\beta) - 3\sin(\beta)] \\ &\quad + \frac{1}{8}e^2R[3\sin(3\alpha-2\beta) - 10\sin(\alpha) \\ &\quad + 5\sin(\alpha-2\beta)] \\ z(t) &= -\sqrt{3}eR\cos(\alpha-\beta) + \sqrt{3}e^2R[\cos^2(\alpha-\beta) \\ &\quad + 2\sin^2(\alpha-\beta)]. \end{aligned} \tag{1}$$

In the above $R=1$ AU. is the radial distance to the guiding center, e is the eccentricity, $\alpha = 2\pi f_m t + \kappa$ is the orbital phase of the guiding center, and $\beta = 2\pi n/3 + \lambda$ $(n=0,1,2)$ is the relative phase of the spacecraft within the constellation. The parameters κ and λ give the initial ecliptic longitude and orientation of the constellation.

Using the above coordinates the instantaneous separations between spacecraft are found to be

$$L_{12}(t)=L\left\{1+\frac{e}{32}\left[15\sin\left(\alpha-\lambda+\frac{\pi}{6}\right)-\cos[3(\alpha-\lambda)]\right]\right\}$$

$$L_{12}(t)=L\left\{1-\frac{e}{32}\left[15\sin\left(\alpha-\lambda-\frac{\pi}{6}\right)+\cos[3(\alpha-\lambda)]\right]\right\}$$

$$L_{23}(t)=L\left\{1-\frac{e}{32}[15\cos(\alpha-\lambda)+\cos[3(\alpha-\lambda)]]\right\}, \tag{2}$$

with $L=2\sqrt{3}\,eR$. From this it is seen that to linear order in the eccentricity the detector arms are rigid. By setting the mean arm length equal to those of the LISA baseline, $L=5\times10^9$ m, the spacecraft orbits are found to have an eccentricity of $e=0.00965$, which indicates that the second order effects are down by a factor of 100 relative to leading order.

B. Gravitational wave description

An arbitrary gravitational wave traveling in the $\hat{k}$ direction can be written as the linear sum of two independent polarization states,

$$\mathbf{h}(\xi)=h_+(\xi)\boldsymbol{\epsilon}^+ + h_\times(\xi)\boldsymbol{\epsilon}^\times, \tag{3}$$

where the wave variable $\xi=t-\hat{k}\cdot\mathbf{x}$ gives the surfaces of constant phase. The polarization tensors are given by

$$\boldsymbol{\epsilon}^+=\cos(2\psi)\mathbf{e}^+-\sin(2\psi)\mathbf{e}^\times$$

$$\boldsymbol{\epsilon}^\times=\sin(2\psi)\mathbf{e}^++\cos(2\psi)\mathbf{e}^\times, \tag{4}$$

where ψ is the principle polarization angle and the basis tensors $\mathbf{e}^+$ and $\mathbf{e}^\times$ are expressed in terms of two orthogonal unit vectors,

$$\mathbf{e}^+=\hat{u}\otimes\hat{u}-\hat{v}\otimes\hat{v}$$

$$\mathbf{e}^\times=\hat{u}\otimes\hat{v}+\hat{v}\otimes\hat{u}. \tag{5}$$

These vectors, along with the propagation direction of the gravitational wave, form an orthonormal triad, which may be expressed as a function of the source location on the celestial sphere (θ,ϕ),

$$\hat{u}=\cos\theta\cos\phi\hat{x}+\cos\theta\sin\phi\hat{y}-\sin\theta\hat{z}$$

$$\hat{v}=\sin\phi\hat{x}-\cos\phi\hat{y}$$

$$\hat{k}=-\sin\theta\cos\phi\hat{x}-\sin\theta\sin\phi\hat{y}-\cos\theta\hat{z}. \tag{6}$$

The above basis set is defined with respect to the barycenter reference frame. For a binary system—the standard gravitational wave source in the LISA band—it is natural to introduce another basis that is aligned with principle polarization axes $\hat{p}$ and $\hat{q}$ of the gravitational radiation. The orientation of the principle directions is chosen such that there is a $\pi/2$ phase delay between the two polarization states. The connection between the two basis sets is a rotation by the principle polarization angle ψ about the shared propagation direction $\hat{k}$.

We model the gravitational waves from a binary system according to

$$h_{+,\times}(\xi)=\sum_n h^{(n)}_{+,\times}e^{in\Psi(\xi)} \tag{7}$$

where $\Psi(\xi)$ is the orbital phase. The instantaneous frequency of the nth gravitational wave harmonic is given by

$$f_n(\xi)=\frac{n}{2\pi}\frac{\partial\Psi}{\partial t}. \tag{8}$$

Unless the binary is highly eccentric or highly relativistic, the dominant emission will be quadrupolar, with frequency $f(\xi)=f_2(\xi)$, and will be well described by the restricted post-Newtonian approximation:

$$h_+(\xi)=\frac{2\mathcal{M}[\pi f(\xi)]^{2/3}}{D_L}(1+\cos^2\iota)\cos2\Psi(\xi)$$

$$h_\times(\xi)=-\frac{4\mathcal{M}[\pi f(\xi)]^{2/3}}{D_L}\cos\iota\sin2\Psi(\xi). \tag{9}$$

Here $\mathcal{M}$ is the chirp mass, D_L is the luminosity distance, and ι is the inclination of the binary to the line of sight. Higher post-Newtonian corrections, eccentricity of the orbit, and spin effects will introduce additional harmonics.

III. DETECTOR RESPONSE: ANALYTICAL

For two spatially separated test particles in free fall, the effect of a passing gravitational wave is to cause the proper distance between the masses to vary as a function of time. Finding the detector response reduces to solving for the appropriate timelike and null geodesics in the spacetime with the metric

$$ds^2=-(1+2\phi)dt^2+(1-2\phi)(dx^2+dy^2+dz^2)+h_{ij}dx^idx^j. \tag{10}$$

In the above equation ϕ denotes the Newtonian potential set up by various bodies in the Solar system and h_{ij} denotes the time-varying metric perturbation due to gravitational waves described in the preceding section. The relevant geodesics are those of the two spacecraft, $\vec{x}_1(\tau_1)$, $\vec{x}_2(\tau_2)$, and the photons sent from spacecraft 1 to 2, $\vec{x}_\nu(\lambda)$. We need to find the path taken by the photon that leaves spacecraft 1 at time t_1 and arrives at spacecraft 2 at time t_2, which amounts to a classic pursuit problem in curved spacetime. The calculation must take into account a host of factors, some due to the Newtonian potential, and some due to the gravitational wave. During the time taken for the photon to travel between the spacecraft, both effects are small and can be treated independently.

The Newtonian potential leads to a variety of effects, such as a Shapiro time delay $\Delta L/L \sim M_\odot/R$, gravitational redshift $\Delta\nu/\nu \sim M_\odot L/R^2$, deflection of light $\Delta\theta \sim M_\odot L/R^2$, and tidal flexing $\Delta L/L \sim M_\odot L^2/R^3$. Each of these effects is considerably larger than any of the effects caused by the passage of the gravitational wave, and they have to be subtracted before the gravitational wave data analysis begins. The first step in the subtraction relies on us being able to accurately model the orbital phase shifts using the solar system ephemeris. The second step in the subtraction employs a high pass filter to remove the residuals from the orbital fit, which occur at harmonics of the modulation frequency $f_m = 1/\mathrm{yr} \simeq 3.2\times10^{-8}$ Hz. The orbital effects, and the procedure for their removal, should be included in the full end-to-end model, even though they do not directly affect the response of the detector to gravitational waves.

The effect of the gravitational wave on the phase shift can be found by setting $\phi=0$ in Eq. (10) and solving the geodesic equation for the photons and the spacecraft in the metric perturbed by the gravitational wave. There are two equivalent approaches for finding the phase shift. The first approach is to find the Doppler shift of the photon emitted by the first spacecraft and received by the second. The Doppler shift is then integrated with respect to time to give the phase shift. The Doppler derivation is given in Appendix B. The second approach is to integrate along the photon's trajectory to find the path length variation caused by the gravitational wave [4]. The expressions given in Appendix B are valid to all orders in the spacecraft velocity v, and to first order in the gravitational wave strain h. However, as we explained in Ref. [4], it is hard to justify keeping terms of order vh given that $v \sim 10^{-4}$. It would take a phenomenally bright source, with a signal to noise ratio of $\sim 10^5$, for the vh cross terms to be noticeable. Working to leading order in v and h, the path length variation for a photon propagating from spacecraft i to spacecraft j is given by

$$\delta\ell_{ij}(t) = \frac{1}{2}\frac{\hat{r}_{ij}(t)\otimes\hat{r}_{ij}(t)}{1-\hat{k}\cdot\hat{r}_{ij}(t)} : \int_{\xi_i}^{\xi_j} \mathbf{h}(\xi)\, d\xi, \tag{11}$$

where $\hat{r}_{ij}(t)$ points from test mass i to mass j and $\mathbf{h}(\xi)$ is the gravitational wave tensor in the transverse-traceless gauge. The colon here denotes a double contraction, $\mathbf{a}:\mathbf{b} = a^{ij}b_{ij}$.

Applying Eq. (11) to a pair of orbiting spacecraft requires the careful evaluation of the $\hat{r}_{ij}(t)$ unit vectors. This calculation is complicated by the motion of the spacecraft and the finite speed of light. For a photon emitted from spacecraft i at time t_i and received at spacecraft j at time t_j the proper evaluation of the unit vectors is

$$\hat{r}_{ij}(t_i) = \frac{\mathbf{x}_j(t_j) - \mathbf{x}_i(t_i)}{\ell_{ij}(t_i)}. \tag{12}$$

The distance the photon travels between spacecraft is given implicitly through the relationship

$$\ell_{ij}(t_i) = \|\mathbf{x}_j[t_i + \ell_{ij}(t_i)] - \mathbf{x}_i(t_i)\|. \tag{13}$$

Here we have used the fact that the reception time is the emission time plus the time of flight for the photon. We can numerically estimate the magnitude of this point ahead effect by expanding the photon propagation distance in a v/c series:

$$\ell_{ij}(t_i) = L_{ij}(t_i)[1 + \hat{r}_{ij}(t_i)\cdot\mathbf{v}_j(t_i) + \mathcal{O}(v^2)], \tag{14}$$

where $\mathbf{v}_j(t_i)$ is the velocity of spacecraft j and

$$L_{ij}(t_i) = \|\mathbf{x}_j(t_i) - \mathbf{x}_i(t_i)\| \tag{15}$$

is the instantaneous spacecraft separation. For the LISA mission with a mean arm length of 5×10^9 m and spacecraft velocity $v \approx 2\pi f_m R \approx 10^{-4}$, pointing ahead gives a first order effect of approximately 10^5 m. For comparison, the orbital effects given in Eq. (2) impart a variation in the photon propagation distance of 10^7 m.

An arbitrary gravitational wave can be decomposed into its frequency components:

$$\mathbf{h}(\xi) = \int_{-\infty}^{\infty} \tilde{\mathbf{h}}(f) e^{2\pi i f\xi} df. \tag{16}$$

Such a decomposition allows us to rewrite Eq. (11) in the form

$$\delta\ell_{ij}(t) = \ell_{ij}(t) \int_{-\infty}^{\infty} \mathbf{D}(f,t,\hat{k}) : \tilde{\mathbf{h}}(f) e^{2\pi i f\xi} df, \tag{17}$$

where the one-arm detector tensor is given by

$$\mathbf{D}(f,t,\hat{k}) = \frac{1}{2}[\hat{r}_{ij}(t)\otimes\hat{r}_{ij}(t)]\mathcal{T}(f,t,\hat{k}), \tag{18}$$

and the transfer function is

$$\mathcal{T}(f,t,\hat{k}) = \mathrm{sinc}\left(\frac{f}{2f^*_{ij}}[1-\hat{k}\cdot\hat{r}_{ij}(t)]\right) \times \exp\left(i\frac{f}{2f^*_{ij}}[1-\hat{k}\cdot\hat{r}_{ij}(t)]\right). \tag{19}$$

Here $f^*_{ij} = 1/(2\pi\ell_{ij})$ is the transfer frequency for the ij arm. The transfer functions arise from the interaction of the gravitational wave with the detector. For gravitational radiation whose frequency is greater than the transfer frequency the wave period is less than the light propagation time between spacecraft, which leads to a self-cancellation effect accounted for by the transfer functions. Below the transfer frequency the transfer functions approach unity. This leads to a natural division of the LISA bandwidth into high and low frequency regions, which will be exploited in a later section when we approximate the response of the detector.

The connection of Eq. (11) to what is actually measured depends on the design of the gravitational wave detector. The current proposal for LISA is to have each spacecraft measure two phase differences, one for each arm. The phase difference $\Phi_{ij}(t_j)$, as measured on spacecraft j, is found by com-

paring the phase of the received signal from spacecraft i against the outgoing signal's phase that is traveling back to spacecraft i. Inherent in the phase difference measurements are both the gravitational wave signal and noise contributions from laser phase noise $C(t)$, shot noise $n^s(t)$, and acceleration noise $n^a(t)$:

$$\Phi_{ij}(t_j) = C_{ji}(t_i) - C_{ij}(t_j) + 2\pi\nu_0[n^s_{ij}(t_j) - n^a_{ij}(t_j) + n^a_{ji}(t_i) + \delta_{ij}\ell(t_i)]. \quad (20)$$

Here the time t_i is implicitly found through $t_i = t_j - \ell_{ij}(t_i)$. The subscripts on the noise components indicate the directional dependence of that component: C_{ij} is the laser phase noise introduced by the laser on spacecraft j that is pointed toward spacecraft i, n^s_{ij} is the shot noise in the photodetector on spacecraft j that is receiving a signal from spacecraft i, and n^a_{ij} is the projected acceleration noise from the accelerometer on spacecraft j in the direction of spacecraft i. The position noise and path length variation are converted into a phase difference by multiplying by the angular frequency of the laser, $2\pi\nu_0$.

Once the six phase differences are measured, the different interferometer signals can be synthesized. For example, the Michelson signal formed by using spacecraft 1 as the vertex craft is

$$S_1(t) = \Phi_{12}(t_{21}) + \Phi_{21}(t) - \Phi_{13}(t_{31}) - \Phi_{31}(t), \quad (21)$$

where t_{21} and t_{31} are found from

$$t_{21} = t - \ell_{21}(t_{21})$$
$$t_{31} = t - \ell_{31}(t_{31}). \quad (22)$$

However, due to the relatively large laser phase noise, the Michelson signal will not be a viable option. Instead a number of so-called TDI signals will be used [5]. These signals are built by combining time-delayed Michelson signals in such a way as to reduce the overall laser phase noise down to a level that will not overwhelm the detector's output. A particular example of a TDI variable is the X signal [20]:

$$X(t) = \Phi_{12}(t_{21}) + \Phi_{21}(t) - \Phi_{13}(t_{31}) - \Phi_{31}(t) - \Phi_{12}(t'_{21}) - \Phi_{21}(t_{13}) + \Phi_{13}(t'_{31}) + \Phi_{31}(t_{12}), \quad (23)$$

where the new times t_{12}, t_{13}, t'_{21}, and t'_{31} are defined through the implicit relationships

$$t_{12} = t_{21} - \ell_{12}(t_{12})$$
$$t_{13} = t_{31} - \ell_{13}(t_{13})$$
$$t'_{21} = t_{13} - \ell_{21}(t'_{21})$$
$$t'_{31} = t_{12} - \ell_{31}(t'_{31}). \quad (24)$$

By permutations of the indices similar forms for the Y and Z signals can be constructed.

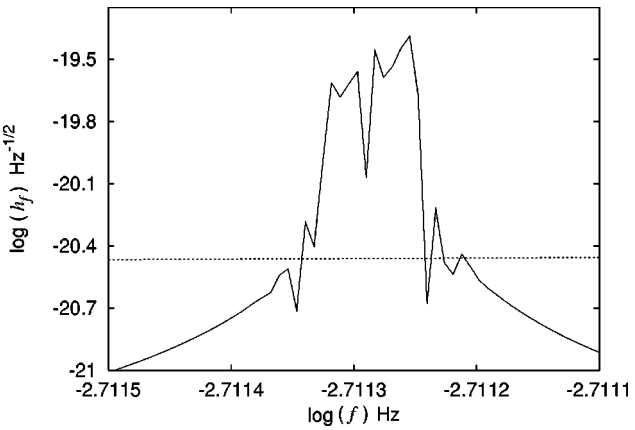

FIG. 2. The simulated X strain spectral density of AM CVn, demonstrating the induced modulations caused by the motion of the detector about the Sun. For reference, the dotted line is the average noise in this region of the spectrum.

By writing the response of the detector in a coordinate free manner we are able to apply this formalism to an arbitrary space-based mission. All that has to be changed are the spacecraft orbits. It should also be emphasized that the response is calculated entirely in the time domain. In later sections we develop approximations to the full response by working in a hybrid time/frequency domain. This hybrid approach assumes extra information about the sources, which allows us to develop explicit expressions for the detector response.

IV. DETECTOR RESPONSE: NUMERICAL

A. Noiseless response

As an application of the equations presented in the previous section, we have simulated the response of the proposed LISA mission. *The LISA Simulator* [14] is designed to take an arbitrary gravitational waveform and output the full response of the detector. To apply the equations we have elected to work entirely in the heliocentric, ecliptic coordinate system. Therefore, all times are evaluated in terms of solar system barycentric (SSB) time. The conversion to the detector time is through the standard relationship $d\tau = \sqrt{1-v^2(t)}dt$, but since we only work to leading order in v the distinction is not made. (In practice there will be difficulties in synchronizing the clocks on the spacecraft [21], but they do not trouble the simulations.)

The positions of the spacecraft are calculated to second order in the eccentricity, Eq. (1), which includes the leading order flexing motion of the array. Tidal effects, and third order terms in the eccentricity, are neglected for now.

One of the guaranteed sources for the LISA mission is the cataclysmic variable AM Canum Venaticorum (AM CVn). This binary star system is comprised of a low mass helium white dwarf that is transferring material to a more massive white dwarf by way of Roche lobe overflow. AM CVn's orbital frequency of 0.972 mHz and close proximity to the Earth ($\sim$100 pc) make it a good calibration binary for LISA. Shown in Fig. 2 is the simulated response to AM CVn ex-

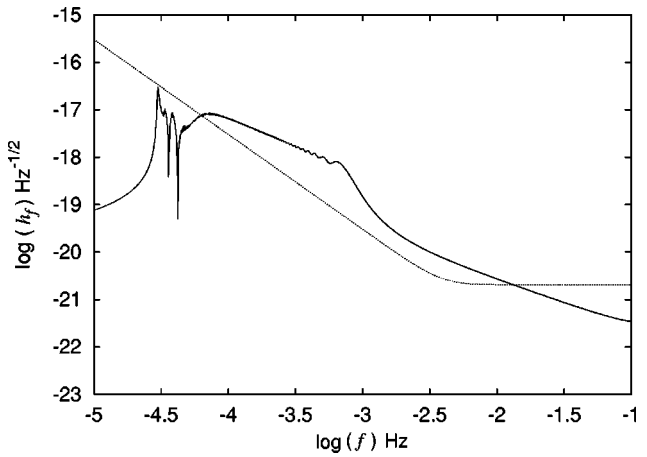

FIG. 3. The Michelson response of LISA to two 10^6 $M_\odot$ black holes coalescing at $z=1$ ($D_L=6.63$ Gpc). The dotted line is the average Michelson noise in the detector.

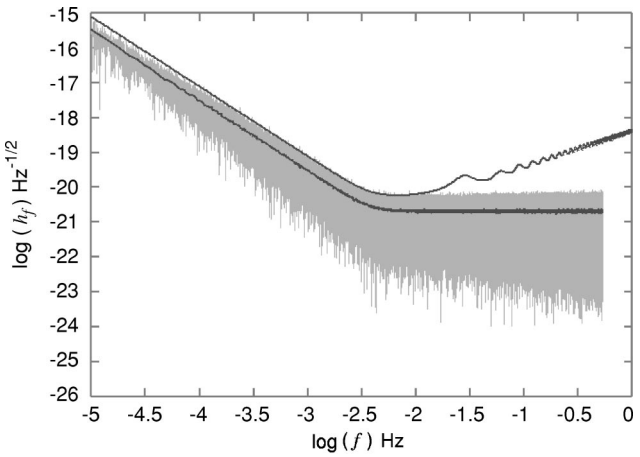

FIG. 4. A realization of the Michelson noise for LISA, expressed here as a strain spectral density. The dark line within the noise is a 128 bin rms value, while the rising curve is a standard LISA sensitivity curve.

pressed as a strain spectral density $h_f(f)$. Note that the barycenter gravitational wave signal will be approximately monochromatic; however, the motion of LISA introduces modulations that cause the signal to spread over a range of frequencies [17].

Another LISA source, but one whose event rate is poorly known, is the merger of two super-massive black holes. Figure 3 shows the simulated response of LISA to two 10^6 $M_\odot$ black holes coalescing at a redshift of $z=1$. The observation tracks the final year before coalescence.

B. Noise

Laser phase noise, photon shot noise, and acceleration noise are expected to be the dominant forms of noise in space-borne detectors. As previously discussed, time delay interferometry is used to reduce the effects of the laser phase noise to a tolerable level. We assume that the TDI signal processing is properly implemented, and therefore we neglect laser phase noise in our simulation.

The simulation of the noise is done in the time domain by drawing random numbers at each time step from a Gaussian distribution with unit variance and zero mean. For the white photon noise we then scale the random number by the shot noise spectral density defined in Ref. [23] ($S_{\rm ps}=1.0\times10^{-22}$ m^2/Hz). For the colored acceleration noise we begin by generating a white noise time series scaled by the acceleration noise spectral density ($S_{\rm acc}=9.0\times10^{-30}$ m^2/s^4/Hz), then integrate it twice to arrive at a colored time series. The integration introduces a f^{-4} falloff in the power spectrum that is characteristic of acceleration noise. The results of this procedure for the Michelson signal are shown in Fig. 4.

Comparing this graph to a standard LISA sensitivity curve [24], a number of differences are apparent. The most obvious one is the lack of rise in the high frequency region. This is because the standard sensitivity curve folds the average detector response into the noise curve. The *Sensitivity Curve Generator* includes the all sky averaged and polarization averaged transfer function, which equals 3/5 at low frequencies and grows as f^2 above the transfer frequency. A secondary difference is in the overall normalization, as the *Sensitivity Curve Generator* scales the path length variations by the interferometer mean arm length of L, while we scale the path length variations by the optical path length of $2L$.

To arrive at a simulation of the X noise we combine the noise elements as dictated by Eq. (23). Doing so gives the results displayed in Fig. 5, which agrees with the predicted results. To see this, we start with the analytical expression of the average Michelson noise curve shown in Fig. 4,

$$h_f^M(f)=\frac{1}{2L}\left\{4S_{\rm ps}+8\left[1+\cos^2\left(\frac{f}{f_*}\right)\right]\frac{S_{\rm acc}}{(2\pi f)^4}\right\}^{1/2} \quad (25)$$

which is derived in the appendix of Ref. [25]. In the above $f_*=1/(2\pi L)$ is the mean transfer frequency for an arm. Next, we note that the X signal is formed by differencing two Michelson signals, one time delayed by roughly twice the light travel time between spacecraft. Therefore, the noise will enter in the X signal as

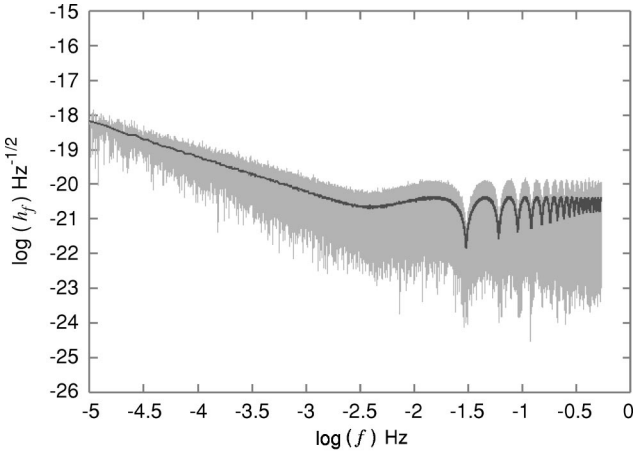

FIG. 5. A realization of the X noise for LISA, expressed here as a strain spectral density. The dark line is a 128 bin rms value for the noise.

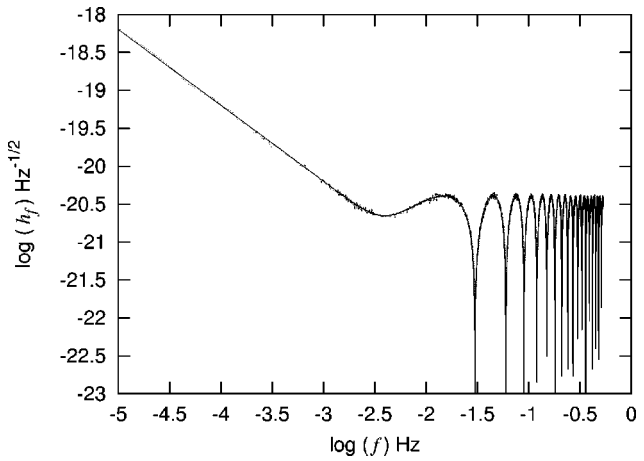

FIG. 6. A comparison of the simulated rms X noise (dotted) to the analytical prediction (solid).

$$n_X(t) = n_M(t) - n_M(t-2L), \tag{26}$$

which has a Fourier transform of

$$\tilde{n}_X(f) = \tilde{n}_M(f)(1 - e^{-2if/f_*}) \tag{27}$$

and a power spectral density of

$$S_X(f) = 4\sin^2\left(\frac{f}{f_*}\right) S_M(f). \tag{28}$$

The strain spectral density of the X noise is given by

$$h_f^X(f) = \sqrt{S_X(f)} = 2\left|\sin\left(\frac{f}{f_*}\right)\right| h_f^M(f). \tag{29}$$

Shown in Fig. 6 is a plot of $h_f^X(f)$ along with the average from Fig. 5. Although the derivation of the X noise strain spectral density assumed constant arm lengths we see that there is excellent agreement between the predicted results of Eq. (29) and the simulation, which included the variations in the arms.

Although Eqs. (11), (20), and (23) give the full response of a space-borne detector, they are analytically difficult to handle and time consuming to evaluate. For this reason we will now explore some approximations to the full response that use information about the input waveforms and a simplified description of the detector. These approximations not only aid in the development of data analysis techniques, but also give a greater insight into the workings of the detector.

V. LOW FREQUENCY APPROXIMATION

In Secs. II and III we saw that the full response of a space-borne gravitational wave detector was complicated by the intrinsic arm-length fluctuations, pointing ahead, and the signal cancellation accounted for in the transfer functions. As a first approximation to the response of LISA we will neglect all of these effects. That is, we will work to linear order in the spacecraft positions, evaluate all spacecraft locations at a common time, and set the transfer functions to unity. It should be noted that this approximation was originally worked out by Cutler [13] and can be viewed as an extension of the LIGO response to space-borne detectors. The transfer function $\mathcal{T}(f,t,\hat{k})$ can be set equal to unity when $f \ll f_*$. For the LISA mission, whose bandwidth is 10^{-5} to 1 Hz, the transfer frequency has a mean value of $f_* = 0.00954 \approx 10^{-2}$ Hz.

In the limit $f \ll f_*$ and $f/\dot{f} \ll L$ the path length variation (11) reduces to

$$\delta\ell_{ij}(t) \simeq \frac{1}{2}\frac{\hat{r}_{ij}(t)\otimes\hat{r}_{ij}(t)}{1-\hat{k}\cdot\hat{r}_{ij}(t)} : \mathbf{h}(\xi(t))(\xi_j - \xi_i) = L[\hat{r}_{ij}(t)\otimes\hat{r}_{ij}(t) : \mathbf{h}(\xi(t))]. \tag{30}$$

Working in terms of strains and neglecting noise, the Michelson signal from spacecraft 1 is given by

$$s_1(t) = \frac{\delta\ell_{12}(t-2L) + \delta\ell_{21}(t-L)}{2L} - \frac{\delta\ell_{13}(t-2L) + \delta\ell_{31}(t-L)}{2L} \simeq \frac{\delta\ell_{12}(t) + \delta\ell_{21}(t) - \delta\ell_{13}(t) - \delta\ell_{31}(t)}{2L}. \tag{31}$$

The last line follows from the condition $f \ll f_*$.

Using Eqs. (3), (7), and (30) the strain can be re-expressed as

$$s_1(t) = h_+(\xi_1(t))F^+ + h_\times(\xi_1(t))F^\times, \tag{32}$$

where

$$\xi_1(t) = t - \hat{k}\cdot\mathbf{x}_1(t) = t + R\sin\theta\cos[\alpha(t) - \phi] \tag{33}$$

is the gravitational wave phase measured at spacecraft 1. The antenna beam pattern factors, $F^+(t)$ and $F^\times(t)$, are given by

$$F^+(t) = \frac{1}{2}[\cos(2\psi)D^+(t) - \sin(2\psi)D^\times(t)]$$

$$F^\times(t) = \frac{1}{2}[\sin(2\psi)D^+(t) + \cos(2\psi)D^\times(t)], \tag{34}$$

where

$$D^+(t) = [\hat{r}_{12}(t)\otimes\hat{r}_{12}(t) - \hat{r}_{13}(t)\otimes\hat{r}_{13}(t)] : \mathbf{e}^+$$

$$D^\times(t) = [\hat{r}_{12}(t)\otimes\hat{r}_{12}(t) - \hat{r}_{13}(t)\otimes\hat{r}_{13}(t)] : \mathbf{e}^\times. \tag{35}$$

Working to linear order in the eccentricity, the Keplerian orbits given in Eq. (1) yield

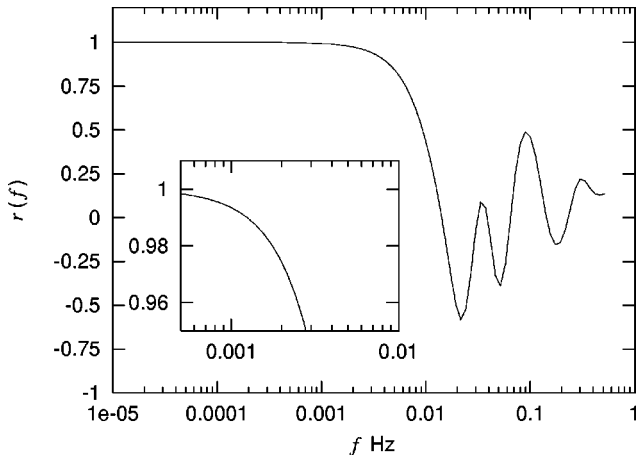

FIG. 7. The correlation between the low frequency approximation and the full response of the LISA detector for a monochromatic source. The oscillatory structure at high frequencies is due to the transfer functions introduced by the full response.

$$D^{+}(t)=\frac{\sqrt{3}}{64}[-36\sin^2(\theta)\sin[2\alpha(t)-2\lambda]+[3+\cos(2\theta)](\cos(2\phi)\{9\sin(2\lambda)-\sin[4\alpha(t)-2\lambda]\}+\sin(2\phi)\{\cos[4\alpha(t)-2\lambda]-9\cos(2\lambda)\})-4\sqrt{3}\sin(2\theta)\{\sin[3\alpha(t)-2\lambda-\phi]-3\sin[\alpha(t)-2\lambda+\phi]\}] \tag{36}$$

and

$$D^{\times}(t)=\frac{1}{16}(\sqrt{3}\cos(\theta)\{9\cos(2\lambda-2\phi)-\cos[4\alpha(t)-2\lambda-2\phi]\}-6\sin(\theta)\{\cos[3\alpha(t)-2\lambda-\phi]+3\cos[\alpha(t)-2\lambda+\phi]\}). \tag{37}$$

Equations (32) to (37) constitute the analytical formalism for the low frequency approximation. These equations are numerically quick to evaluate and can be handled analytically. As a point of reference, the strain presented in Eq. (32) can be shown to be equivalent (most easily through a numerical comparison) to that derived by Cutler [13].

To test the range of validity of this approximation we used *The LISA Simulator* (TLS) as a template to calculate the correlation between the full response and the low frequency approximation (LFA),

$$r(f)=\frac{\langle s_{\rm TLS}|s_{\rm LFA}\rangle}{\sqrt{\langle s^2_{\rm TLS}\rangle\langle s^2_{\rm LFA}\rangle}}. \tag{38}$$

Using fixed random choices for the source location and orientation we systematically varied the gravitational wave frequency and calculated the correlation at each frequency. The results of this calculation are shown in Fig. 7.

We found that the low frequency approximation has a strong correlation to the true response for frequencies below 3 mHz, at which point the correlation drops to 95%. The steep turn down in the correlation as the transfer frequency is approached is to be expected as the low frequency approximation neglects the self-cancellation effects encoded in the transfer functions. The wiggles at higher frequencies are due to the transfer functions present in the full response template $s_{\rm TLS}$. The precise structure of these oscillations depends on the source location through the $\hat{k}\cdot\hat{r}_{ij}(t)$ dependence in the transfer functions. However, the turn down at 3 mHz is location independent. The location dependence does not become strongly evident until the correlation value has dropped to roughly zero.

The significance of a particular correlation value is dependent on the signal-to-noise (S/N) ratio of the source. For high S/N the effects neglected in the approximation will be detectable. Conversely, for a low S/N one may continue to use the approximation at higher frequencies as the difference would not be noticeable.

VI. RIGID ADIABATIC APPROXIMATION

A. Response formalism

The breakdown of the low frequency approximation comes about through neglecting the transfer functions. As a second approximation to the LISA response we will now include the transfer functions, but continue to hold the detector rigid by working to leading order in the spacecraft positions and evaluating all spacecraft locations at the same instant of time. Such an approximation has been worked out before for the case of a stationary detector in [25,26], but here we extend it to include the motion of the detector.

Physically this approximation can be viewed in the following way. At an instant of time we hold the detector fixed and send photons up and back along the interferometer arms and calculate the phase difference. We then increment the time by a small amount, moving the rigid detector to its new position in space, and repeat the process. This sequence of stationary states is the origin of the term ''adiabatic'' for describing the approximation.

For chirping sources the adiabatic approximation requires that the frequency evolution $\dot{f}$ occurs on a time scale long compared to the light travel time in the interferometer: $f/\dot{f}\ll L$. When this condition does not hold the rigid adiabatic approximation is no longer valid and the full response should be used. In the limit $f/\dot{f}\ll L$ the path length variation (11) reduces to

$$\delta\ell_{ij}(\xi)=L\sum_n \mathbf{D}(f_n,t,\hat{k}):\mathbf{h}_n(\xi), \tag{39}$$

where the one-arm detector tensor is given by

$$\mathbf{D}(f,t,\hat{k})=\frac{1}{2}[\hat{r}_{ij}(t)\otimes\hat{r}_{ij}(t)]\mathcal{T}(f,t,\hat{k}), \tag{40}$$

and the transfer function is

$$\mathcal{T}(f,t,\hat{k}) = \mathrm{sinc}\left(\frac{f}{2f_*}[1-\hat{k}\cdot\hat{r}_{ij}(t)]\right) \times \exp\left(i\frac{f}{2f_*}[1-\hat{k}\cdot\hat{r}_{ij}(t)]\right). \quad (41)$$

The Michelson signal is given by

$$s_1(t) = \frac{\delta\ell_{12}(t-2L)+\delta\ell_{21}(t-L)}{2L} - \frac{\delta\ell_{13}(t-2L)+\delta\ell_{31}(t-L)}{2L}, \quad (42)$$

which may now be expressed as

$$s_1(t) = \sum_n \mathbf{D}(\hat{k},f_n):\mathbf{h}_n(\xi), \quad (43)$$

and the round-trip detector tensor takes the form

$$\mathbf{D}(\hat{k},f) = \frac{1}{2}[(\hat{a}\otimes\hat{a})\mathcal{T}(\hat{a}\cdot\hat{k},f) - (\hat{b}\otimes\hat{b})\mathcal{T}(\hat{b}\cdot\hat{k},f)], \quad (44)$$

and the round-trip transfer function is

$$\mathcal{T}(\mathbf{a}\cdot\hat{k},f) = \frac{1}{2}\left[\mathrm{sinc}\left(\frac{f(1-\hat{a}\cdot\hat{k})}{2f_*}\right)\exp\left(-i\frac{f}{2f_*}(3+\hat{a}\cdot\hat{k})\right) + \mathrm{sinc}\left(\frac{f(1+\hat{a}\cdot\hat{k})}{2f_*}\right)\exp\left(-i\frac{f}{2f_*}(1+\hat{a}\cdot\hat{k})\right)\right]. \quad (45)$$

The time-dependent unit vectors, $\hat{a}(t)$ and $\hat{b}(t)$, are given by

$$\hat{a}(t) = \frac{\mathbf{x}_2(t)-\mathbf{x}_1(t)}{L}$$

$$\hat{b}(t) = \frac{\mathbf{x}_3(t)-\mathbf{x}_1(t)}{L}. \quad (46)$$

Collectively these equations are the analytical formalism for the rigid adiabatic approximation. As with the low frequency approximation, the expressions are computationally quick to evaluate and can be easily manipulated analytically.

Figure 8 shows the correlation between the full response and the rigid adiabatic approximation for a monochromatic gravitational wave. Note that by including the transfer functions we are able to extend agreement with the full response two decades in frequency beyond where the low frequency approximation broke down. The turn down at ~ 0.5 Hz comes about through neglecting the second order terms in the spacecraft positions. As we described in Sec. II A the second order orbital effects are down by two orders of magnitude in comparison to the linear order. This shows up in the rigid adiabatic approximation through the transfer frequencies, which are evaluated for a rigid detector. Normally the transfer frequencies are given by

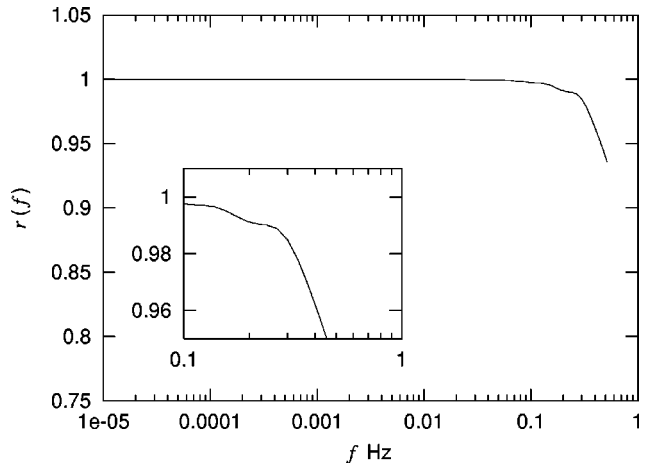

FIG. 8. The correlation between the rigid adiabatic approximation and the full response of the LISA detector. The turn down at ~ 500 mHz is due to neglecting the higher order effects in the spacecraft positions.

$$f^*_{ij}(t) = \frac{1}{2\pi\ell_{ij}(t)}, \quad (47)$$

but for a rigid detector this reduces to the static form $f_* = 1/(2\pi L)$. The extension to higher orders in the orbital eccentricity can be done. The trade off is that the expressions become more complicated since the transfer frequencies would then become functions of time. In turn, this would require that each transfer frequency be evaluated along each arm during each time step rather than using one constant value throughout the entire calculation. Additionally, the normalization of the unit vectors in Eq. (46) would need to be evaluated at each step since the arm lengths would vary as a function of time via Eq. (2). Such an approach would be appropriately called the flexing adiabatic approximation since the arm lengths would now oscillate in time about a mean value of L. Although the expressions would become analytically complicated, the numerical evaluation would not be significantly slower since the additional steps are straightforward to evaluate.

Figure 9 compares the output of *The LISA Simulator* to the rigid adiabatic approximation for a binary system of intermediate mass black holes, each of mass $5000M_\odot$ at a redshift of $z=1$. The observation covers the final year before coalescence. The agreement is excellent. It is worth pointing out that while the raw signal-to-noise ratio at a given frequency f, which is defined in terms of the power spectral density of the source $S_h(f)$ and the power spectral density of the noise $S_n(f)$,

$$\mathrm{SNR}(f) = \sqrt{\frac{S_h(f)}{S_n(f)}}, \quad (48)$$

never exceeds unity for this source, the signal-to-noise ratio that can be achieved by coherent integration against a matched filter [13],

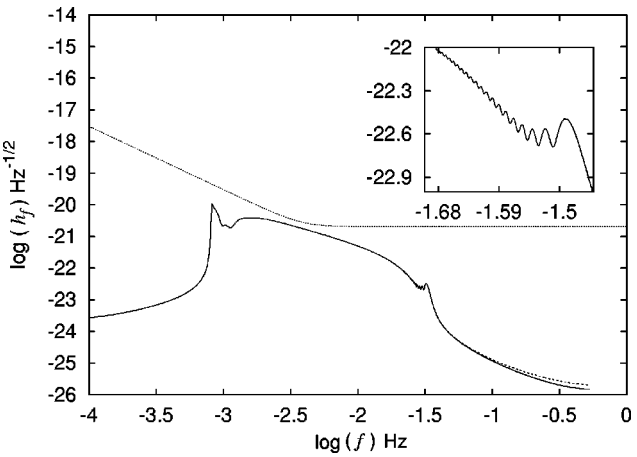

FIG. 9. A comparison of strain spectral densities as calculated using the rigid adiabatic approximation (dashed) and the full response (solid) for a $5000M_\odot$ intermediate mass black hole binary at $z=1$. For reference, the dotted line is the average Michelson noise in the detector.

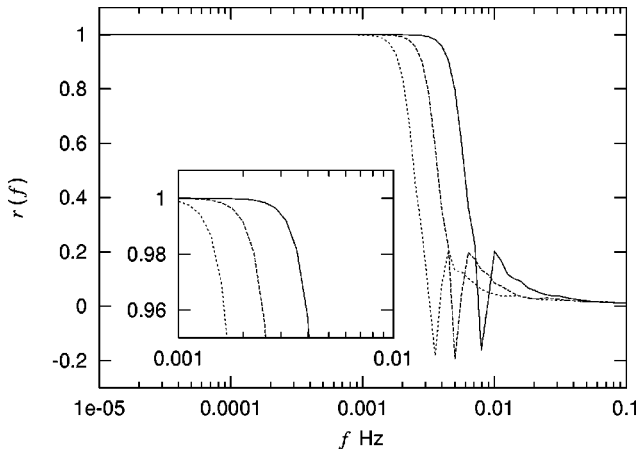

FIG. 10. The correlation between a monochromatic rigid adiabatic approximation and one that includes a 2PN phase evolution. The solid line represents a WD-WD binary with mass components of $0.5M_\odot$, the dashed line is for a NS-NS binary with masses $1.4M_\odot$, and the dotted line is for a $10M_\odot$ black hole and a $1.4M_\odot$ neutron star binary.

$$\mathrm{SNR}_{\mathrm{Wiener}}=\left(\int \frac{2TS_h(f)df}{S_n(f)}\right)^{1/2} \tag{49}$$

is very much greater than unity. During the last year of inspiral, the source shown in Fig. 9 could be detected with an optimally filtered signal-to-noise ratio of over 400.

In a recent paper [27], Seto used a variant of the rigid adiabatic approximation to calculate the effects of LISA's finite arm-lengths on the analysis of gravitational waves from chirping supermassive binary black holes. A comparison of our rigid adiabatic approximation, which is derived from the path length variation, and Seto's approach, which is based on the Doppler shift formalism, is given in Appendix C.

B. Applications

Utilizing the speed of the rigid adiabatic approximation we may investigate various data analysis questions. Here we provide one concrete example by determining when phase evolution of a binary system due to radiation reaction needs to be included in the source modeling.

For our calculations we used the restricted post-Newtonian approximation, whereby the gravitational wave amplitude is calculated to zeroth order while the phase evolution is calculated to second order [29]. The justification for this is that LISA will be far more sensitive to the phase than the amplitude [13]. The lack of additional harmonics of the orbital period also simplifies the calculation as we only have to calculate a single transfer function at each time step.

To quantify the importance of including the evolution of the gravitational wave phase, we calculated the correlation between a monochromatic rigid adiabatic approximation to one in which the phase evolution is included. Figure 10 shows the correlation for three types of binaries expected to reside inside our own galaxy: a white dwarf (WD) binary with mass components $0.5M_\odot$, a neutron star (NS) binary with masses $1.4M_\odot$, and a $10M_\odot$ black hole with a neutron star companion.

What we found is that the frequency at which the monochromatic signal diverges from one that includes phase evolution depends on the masses of the binary components. The reason for this comes from the expression for $\dot{f}$, which contains a mass-dependent coefficient. For the stellar mass binaries we studied, the drop in the correlation happened to coincide with the breakdown of the low frequency approximation. The majority of Milky Way sources have frequencies below 3 mHz, and can be modeled as monochromatic sources using the low frequency approximation. However, the majority of the *resolvable* sources have frequencies above 3 mHz, and these must be modeled as chirping systems using either the full detector response or the rigid adiabatic approximation.

Another way to represent the same data is to map the initial frequency to the time of coalescence. The results of this calculation are shown in Fig. 11. In this case we see that chirping becomes important for stellar mass sources within $\sim 10^5$ years of coalescence. As expected, the mapping to the new variable preserves the mass dependence seen in Fig. 10.

A final way to represent this data is to set the independent variable equal to the change in the frequency scaled by a bin width, $\delta f=(f_f-f_i)/\Delta f$, where for one year of observation the bin width is $\Delta f=1/\mathrm{yr}\simeq 3.2\times 10^{-8}$ Hz. Such an approach is shown in Fig. 12. Unlike with the other representations of the correlation between a monochromatic and coalescing signal, the results of this calculation are independent of the system's masses. It is also interesting to note that this result implies that it will be possible to detect if a source is coalescing or not well within a bin width. This fact is not in conflict with the Nyquist theorem, which states that the frequency resolution will not be better than the inverse of the observation time. The reason is that we have additional information, namely the functional form of the phase

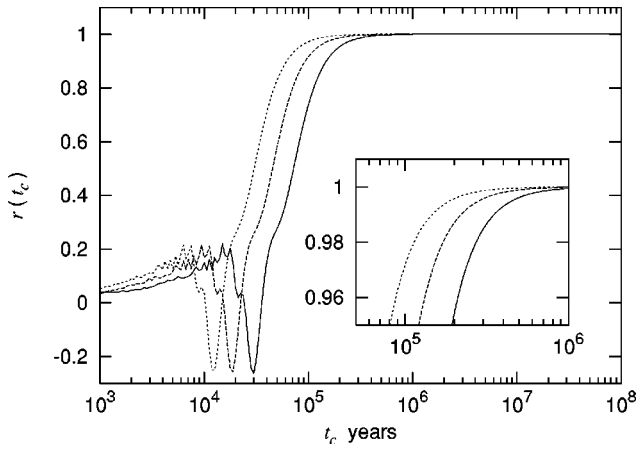

FIG. 11. The correlation between a monochromatic rigid adiabatic approximation and one that includes a 2PN phase evolution, this time expressed in terms of the time to coalescence.

evolution, which is not assumed in deriving Nyquist's theorem.

VII. DISCUSSION

We have examined the forward modeling of space-borne gravitational wave detectors with special emphasis on the LISA observatory. Forward modeling will play two distinct roles in the development of space-borne observatories. The first is as part of a complete end-to-end model that takes into account every conceivable physical effect, and the second is as an intermediary between source simulation and data analysis. Here we have focused on the latter role, and to that end we have studied two simple approximations to the full response, the low frequency approximation and the rigid adiabatic approximation. We found that the rigid adiabatic approximation could be used in place of the full response for a wide range of data analysis projects. For example, the relatively simple analytic form of the rigid adiabatic approximation is well suited to the calculation of Fisher information matrices in studies of astrophysical parameter extraction. On the other hand, *The LISA Simulator* is available if we need to simulate the response to highly relativistic gravitational wave sources such as the merger of two black holes.

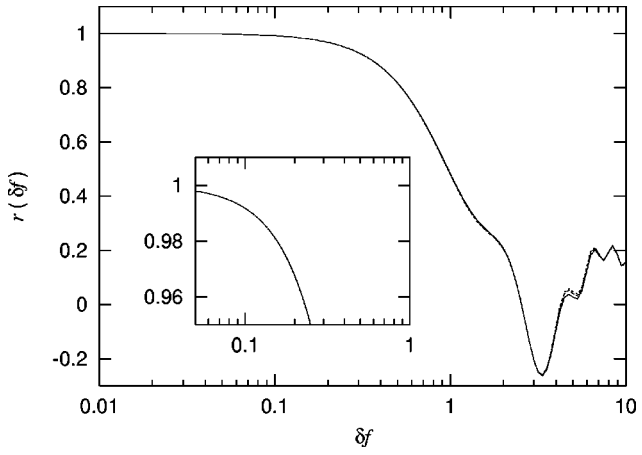

FIG. 12. The correlation as a function of the fractional bin width change in the frequency, $\delta f=(f_f-f_i)/\Delta f$, between a monochromatic rigid adiabatic approximation and one that includes a 2PN phase evolution. Note that all three types of sources previously considered are included in this plot.

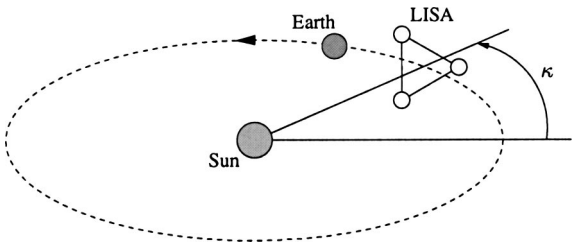

FIG. 13. The angle κ gives the initial ecliptic longitude of the guiding center.

ACKNOWLEDGMENT

We would like to thank Ron Hellings for a number of helpful discussions concerning the simulation of the LISA noise and the removal of orbital effects.

APPENDIX A: SPACECRAFT POSITIONS

For a constellation of spacecraft in individual Keplerian orbits with an inclination of $i=\sqrt{3}e$ the coordinates of each spacecraft are given by the expressions

$$x=r[\cos(\sqrt{3}e)\cos\beta\cos\gamma-\sin\beta\sin\gamma]$$

$$y=r[\cos(\sqrt{3}e)\sin\beta\cos\gamma+\cos\beta\sin\gamma]$$

$$z=-r\sin(\sqrt{3}e)\cos\gamma \tag{A1}$$

where $\beta=2n\pi/3+\lambda$ $(n=0,1,2)$ is the relative orbital phase of each spacecraft in the constellation, γ is the ecliptic longitude, and r is the standard Keplerian radius

$$r=\frac{R(1-e^2)}{1+e\cos\gamma}. \tag{A2}$$

Here R is the semi-major axis of the guiding center and has an approximate value of 1 AU. See Figs. 13 and 14.

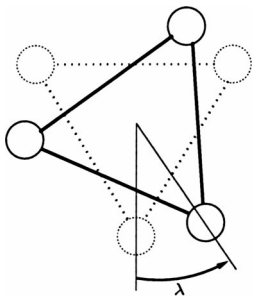

FIG. 14. As viewed by an observer at the origin, λ gives the initial orientation of the spacecraft constellation.

To get the above coordinates as a function of time we first note that the ecliptic longitude is related to the eccentric anomaly ψ by

$$\tan\left(\frac{\gamma}{2}\right)=\sqrt{\frac{1+e}{1-e}}\tan\left(\frac{\psi}{2}\right), \tag{A3}$$

and the eccentric anomaly is related to the orbital phase $\alpha(t)=2\pi t/T+\kappa$ via Kepler's equation

$$\alpha-\beta=\psi-e\sin\psi. \tag{A4}$$

Assuming a small eccentricity we may solve Eq. (A4) through an iterative process where we treat the $e\sin\psi$ term as being lower order than ψ,

$$\psi_n=\alpha-\beta+e\sin\psi_{n-1}. \tag{A5}$$

Through such a procedure we arrive at

$$\psi=\alpha-\beta+e\sin(\alpha-\beta)+e^2\cos(\alpha-\beta)\sin(\alpha-\beta)+\cdots. \tag{A6}$$

Substituting this result into Eq. (A3) and expanding to second order in the eccentricity gives an ecliptic longitude of

$$\gamma=(\alpha-\beta)+2e\sin(\alpha-\beta)+\frac{5}{2}e^2\cos(\alpha-\beta)\sin(\alpha-\beta)+\cdots. \tag{A7}$$

Substituting the ecliptic longitude series into Eq. (A1) and keeping terms up to order e^2 gives the Cartesian positions of the spacecraft as functions of time,

$$\begin{aligned}x(t)=&R\cos(\alpha)+\frac{1}{2}\mathrm{Re}[\cos(2\alpha-\beta)-3\cos(\beta)]\\&+\frac{1}{8}\mathrm{Re}^2[3\cos(3\alpha-2\beta)-10\cos(\alpha)\\&-5\cos(\alpha-2\beta)]\\y(t)=&R\sin(\alpha)+\frac{1}{2}\mathrm{Re}[\sin(2\alpha-\beta)-3\sin(\beta)]\\&+\frac{1}{8}\mathrm{Re}^2[3\sin(3\alpha-2\beta)-10\sin(\alpha)\\&+5\sin(\alpha-2\beta)]\\z(t)=&-\sqrt{3}\,\mathrm{Re}\cos(\alpha-\beta)+\sqrt{3}\,\mathrm{Re}^2[\cos^2(\alpha-\beta)\\&+2\sin^2(\alpha-\beta)].\end{aligned} \tag{A8}$$

These are the desired coordinates of each spacecraft as a function of time.

APPENDIX B: DOPPLER STYLE DERIVATION OF THE FULL RESPONSE

The Doppler shift of a photon emitted by spacecraft 1 and received by spacecraft 2 can be elegantly derived [8] using the symmetries of the spacetime (10). When $\phi=0$ the spacetime admits three Killing vectors,

$$\vec{\zeta}_{(1)}=\hat{u},\quad \vec{\zeta}_{(2)}=\hat{v},\quad \vec{\zeta}_{(3)}=\vec{\partial}_t+\hat{k}. \tag{B1}$$

These provide three constants of the motion, $\vec{\zeta}_{(i)}\cdot\vec{U}$, which along with the normalization condition $\vec{U}\cdot\vec{U}=0$ or $\vec{U}\cdot\vec{U}=-1$ fully specify $\vec{U}(\lambda)$ in terms of some initial four-velocity $\vec{U}(0)$. Writing the metric as $g_{\mu\nu}=\eta_{\mu\nu}+h_{\mu\nu}$, we may express the photon propagation four-vector as

$$\sigma^\mu=s^\mu-\frac{1}{2}\eta^{\mu\alpha}h_{\alpha\beta}s^\beta, \tag{B2}$$

where $\vec{s}$ is a null vector in the unperturbed geometry: $s^\mu s^\nu\eta_{\mu\nu}=0$. At the time of emission from spacecraft 1, $\vec{s}(t_1)=\vec{s}_0+\delta\vec{s}_1$, while at the time of reception at spacecraft 2, $\vec{s}(t_2)=\vec{s}_0+\delta\vec{s}_2$. Here $\vec{s}_0$ is parallel to the unit vector connecting the two spacecraft in the unperturbed spacetime, while $\delta\vec{s}_1$ and $\delta\vec{s}_2$ are perturbations to the path due to lensing by the gravitational wave. Defining

$$\begin{aligned}\Delta s^\alpha&=s^\alpha(t_2)-s^\alpha(t_1),\\\Delta h_{\alpha\beta}&=h_{\alpha\beta}(t_2)-h_{\alpha\beta}(t_1),\end{aligned} \tag{B3}$$

we have

$$\begin{aligned}\sigma^\alpha(t_2)&=\sigma^\alpha(t_1)+\Delta s^\alpha-\frac{1}{2}\eta^{\alpha\beta}\Delta h_{\beta\gamma}s^\gamma\\g_{\alpha\beta}(t_2)&=g_{\alpha\beta}(t_1)+\Delta h_{\alpha\beta}\end{aligned} \tag{B4}$$

which yields

$$\begin{aligned}2s^\alpha\Delta s^\beta\eta_{\alpha\beta}&=\sigma^\alpha(t_2)\sigma^\beta(t_2)g_{\alpha\beta}(t_2)-\sigma^\alpha(t_1)\sigma^\beta(t_1)g_{\alpha\beta}(t_1)\\&=0.\end{aligned} \tag{B5}$$

Equations (B1), (B3) and (B5) yield four equations for the four Δs^α:

$$\begin{aligned}\zeta^\alpha_{(i)}\Delta s^\beta\eta_{\alpha\beta}&=-\frac{1}{2}s_0^\alpha\zeta^\beta_{(i)}\Delta h_{\alpha\beta}\\s_0^\alpha\Delta s^\beta\eta_{\alpha\beta}&=0.\end{aligned} \tag{B6}$$

These can be solved to give, for example,

$$\Delta s^t=-\frac{s_0^i s_0^j\Delta h_{ij}}{2\vec{k}\cdot\vec{s}}. \tag{B7}$$

Here $\vec{k}\to(1,\hat{k})$ is the null propagation vector for the gravitational wave. The frequencies of the emitted and received

photons, as measured at spacecraft 1 and spacecraft 2, are given by $\nu_1 = -\vec{U}_1(t_1)\cdot\vec{\sigma}(t_1)$ and $\nu_2 = -\vec{U}_2(t_2)\cdot\vec{\sigma}(t_2)$, respectively. Here $\vec{U}_1$ and $\vec{U}_2$ are the four-velocities of the two spacecraft. Note the $\nu_1 = \nu_0$ is the operating frequency of the laser on board spacecraft 1. Evaluating $\nu = -\vec{U}\cdot\vec{\sigma}$ yields

$$\nu = -\gamma(t)\left(s^t(t) + v_1^i(t)s^j(t)\eta_{ij} + \frac{1}{2}h_{ij}(t)v^i(t)s_0^j \right) \tag{B8}$$

where $U^t = \gamma = dt/d\tau$ and the v^i are the ordinary three velocities of the spacecraft. The spacecraft trajectories $\vec{U}$ may be expressed in terms of the unperturbed trajectories $\vec{U}_0$ according to

$$U^\alpha = U_0^\alpha + \eta^{\alpha i}h_{ij}U_0^j + A^\alpha, \tag{B9}$$

where A^α are constants set by the initial conditions at some time t. Once the initial conditions for the spacecraft have been set, Eqs. (B6), (B8) and (B9) give the full Doppler shift $\nu_2 - \nu_1$ at any subsequent time. The expressions simplify considerably if we drop terms of order v^2, vh and higher:

$$\Delta\nu = \nu_2 - \nu_1 \simeq \Delta s^t = -\frac{s_0^i s_0^j \Delta h_{ij}}{2\vec{k}\cdot\vec{s}_0}. \tag{B10}$$

Converting this into a fractional frequency shift, $\Delta\nu/\nu_0$, and using $\mathbf{s}_0 = \nu_0\hat{a}$, where $\hat{a}$ is the unit vector connecting the two spacecraft in the background geometry, we have

$$\frac{\Delta\nu}{\nu_0} = \frac{\hat{a}\otimes\hat{a}:\Delta\mathbf{h}}{2(1-\hat{k}\cdot\hat{a})}. \tag{B11}$$

Integrating the above expression with respect to time yields the time delay described by Eq. (11).

APPENDIX C: RECONCILIATION BETWEEN ALTERNATIVE RIGID ADIBATIC FORMALISMS

According to Eq. (2.2) of Ref. [28], the relative frequency shift for a photon traveling from spacecraft 2 to spacecraft 1 can be expressed as

$$y_{31}(t) = \frac{1}{2}[A_+\cos(2\psi_{12}) + iA_\times\sin(2\psi_{12})](1-\cos\theta_{12}) \times[U(t,1) - U(t-L,2)], \tag{C1}$$

where the function $U(t,i)$ gives the phase of the gravitational wave at spacecraft i, θ_{ij} is the angle between the source location on the sky, $-\hat{k}$, and the detector arm $\mathbf{x}_i - \mathbf{x}_j$,

$$\cos\theta_{ij} = -\hat{k}\cdot\hat{r}_{ji}, \tag{C2}$$

and ψ_{ij} is given through the relationship

$$\tan\psi_{ij} = \frac{\hat{r}_{ji}\cdot\hat{q}}{\hat{r}_{ji}\cdot\hat{p}}. \tag{C3}$$

Here $\hat{p}$ and $\hat{q}$ are unit vectors along the principle polarization axes of the gravitational wave. The amplitude coefficients A_+ and $A_\times$ are given as functions of the orbital inclination angle ι and the intrinsic amplitude A,

$$A_+ = A(1+\cos^2\iota)$$
$$A_\times = 2A\cos\iota. \tag{C4}$$

By direct substitution of Eqs. (C2), (C3), and (C4) into the relative frequency shift we arrive at

$$y_{31}(t) = \frac{1-(\hat{k}\cdot\hat{r}_{21})^2}{(\hat{r}_{21}\cdot\hat{p})^2 + (\hat{r}_{21}\cdot\hat{q})^2}\{A_+[(\hat{r}_{21}\cdot\hat{p})^2 - (\hat{r}_{21}\cdot\hat{q})^2] + 2iA_\times(\hat{r}_{21}\cdot\hat{p})(\hat{r}_{21}\cdot\hat{q})\}\frac{U(t,1) - U(t-L,2)}{2(1-\hat{k}\cdot\hat{r}_{21})}. \tag{C5}$$

The overall coefficient

$$\frac{1-(\hat{k}\cdot\hat{r}_{21})^2}{(\hat{r}_{21}\cdot\hat{p})^2 + (\hat{r}_{21}\cdot\hat{q})^2} \tag{C6}$$

can be shown to equal unity by writing the vector $\hat{r}_{ij}$ in terms of the orthonormal triad $\{\hat{p},\hat{q},\hat{k}\}$ according to

$$\hat{r}_{ij} = \sin\theta'\cos\phi'\hat{p} + \sin\theta'\sin\phi'\hat{q} + \cos\theta'\hat{k}. \tag{C7}$$

To proceed further we note that the gravitational wave basis tensors can be expressed as functions of $\hat{p}$ and $\hat{q}$,

$$\boldsymbol{\epsilon}^+ = \hat{p}\otimes\hat{p} - \hat{q}\otimes\hat{q}$$
$$\boldsymbol{\epsilon}^\times = \hat{p}\otimes\hat{q} + \hat{q}\otimes\hat{p}. \tag{C8}$$

Using these relationships, it follows that

$$(\hat{r}_{ij}\otimes\hat{r}_{ij}):\boldsymbol{\epsilon}^+ = (\hat{r}_{ij}\cdot\hat{p})^2 - (\hat{r}_{ij}\cdot\hat{q})^2 \tag{C9}$$

$$(\hat{r}_{ij}\otimes\hat{r}_{ij}):\boldsymbol{\epsilon}^\times = 2(\hat{r}_{ij}\cdot\hat{p})(\hat{r}_{ij}\cdot\hat{q}). \tag{C10}$$

Returning to the expression for the relative frequency shift we now have

$$y_{31}(t) = \frac{\hat{r}_{21}\otimes\hat{r}_{21}}{2(1-\hat{k}\cdot\hat{r}_{21})}:(A_+\boldsymbol{\epsilon}^+ + iA_\times\boldsymbol{\epsilon}^\times) \times[U(t,1) - U(t-L,2)] = \frac{\hat{r}_{21}\otimes\hat{r}_{21}:\Delta\mathbf{h}}{2(1-\hat{k}\cdot\hat{r}_{21})}, \tag{C11}$$

where in the last step we combined the amplitude and phase functions to form the difference in the gravitational wave evaluated at each spacecraft. The above results agrees with Eq. (B11) found in Appendix B.

[1] A. Abramovici *et al.*, Science **256**, 325 (1992).
[2] R. L. Savage *et al.*, prepared for 2nd Workshop on Gravitational Wave Detection, Tokyo, Japan, 1999; B. Abbott *et al.*, gr-qc/0308043.
[3] S. Vitale *et al.*, Nucl. Phys. B (Proc. Suppl.) **110**, 209 (2002).
[4] N.J. Cornish and L.J. Rubbo, Phys. Rev. D **67**, 022001 (2003).
[5] M. Tinto and J.W. Armstrong, Phys. Rev. D **59**, 102003 (1999); F.B. Estabrook, M. Tinto, and J.W. Armstrong, *ibid.* **62**, 042002 (2000).
[6] S.M. Merkowitz, Class. Quantum Grav. **20**, S255 (2003).
[7] E. S. Phinney *et al.*, ''Beyond Einstein: From the Big Bang to Black Holes,'' NASA SEU 2003 Roadmap, universe.gsfc.nasa.gov/be/roadmap.html.
[8] F.B. Estabrook and H.D. Wahlquist, Gen. Relativ. Gravit. **6**, 439 (1975).
[9] R. Schilling, Class. Quantum Grav. **14**, 1513 (1997).
[10] S.L. Larson, W.A. Hiscock, and R.W. Hellings, Phys. Rev. D **62**, 062001 (2000).
[11] F.B. Estabrook, M. Tinto, and J.W. Armstrong, Phys. Rev. D **62**, 042002 (2000); M. Tinto, D.A. Shaddock, J. Sylvestre, and J.W. Armstrong, *ibid.* **67**, 122003 (2003).
[12] S.L. Larson, R.W. Hellings, and W.A. Hiscock, Phys. Rev. D **66**, 062001 (2002).
[13] C. Cutler, Phys. Rev. D **57**, 7089 (1998).
[14] N. J. Cornish, L. J. Rubbo, and O. Poujade, ''The LISA Simulator,'' 2003, www.physics.montana.edu/LISA/.
[15] T.A. Moore and R.W. Hellings, Phys. Rev. D **65**, 062001 (2002).
[16] N.J. Cornish and S.L. Larson, Class. Quantum Grav. **20**, S163 (2003).
[17] N.J. Cornish and S.L. Larson, Phys. Rev. D **67**, 103001 (2003).
[18] J.W. Armstrong, F.B. Estabrook, and M. Tinto, Class. Quantum Grav. **20**, S283 (2003).
[19] D.A. Shaddock, Phys. Rev. D **69**, 022001 (2004).
[20] N.J. Cornish and R.W. Hellings, Class. Quantum Grav. **20**, 4851 (2003).
[21] M. Tinto, F.B. Estabrook, and J.W. Armstrong, gr-qc/0310017.
[22] D.A. Shaddock, M. Tinto, F.B. Estabrook, and J.W. Armstrong, Phys. Rev. D **68**, 061303 (2003).
[23] P. L. Bender *et. al.*, LISA Pre-Phase A Report, 1998.
[24] S. L. Larson, ''Sensitivity Curves for Spaceborne Gravitational Wave Observatories,'' 2003, www.srl.caltech.edu/~shane/sensitivity/index.html.
[25] N.J. Cornish, Phys. Rev. D **65**, 022004 (2001).
[26] N.J. Cornish and S.L. Larson, Class. Quantum Grav. **18**, 3473 (2001).
[27] N. Seto, Phys. Rev. D **66**, 122001 (2002).
[28] N. Seto, Phys. Rev. D **69**, 022002 (2004).
[29] L. Blanchet, B.R. Iyer, C.M. Will, and A.G. Wiseman, Class. Quantum Grav. **13**, 575 (1996).